Article

AMERICAN SCIENTIFIC PUBLISHERS

Journal of
Nanoscience and Nanotechnology
Vol. 16, 4846–4850, 2016
www.aspbs.com/jnn

Boron Oxygen Pair Effect in *p*+ Emitter and Nanosized Boron Rich Layer by Fold Coordination Analysis for Crystalline Silicon Solar Cell Applications

Cheolmin Park[1], Bonggi Kim[2], Nagarajan Balaji[1], Youn-Jung Lee[2], Minkyu Ju[2],
Hoongjoo Lee[3], and Junsin Yi[1,2,*]

[1] *Department of Energy Science, Sungkyunkwan University, Suwon, 440-746, Korea*
[2] *School of Electronic Electrical Engineering, College of Information and Communication Engineering, Sungkyunkwan University, Suwon, 440-746, Korea*
[3] *Department of Computer System Engineering, Sangmyung University, Cheonan 330-720, Korea*

N-type substrates possess better material characteristics than *p*-type substrates for high efficiency mass producible Si solar cells with HIT, IBC structures. The major drawbacks of these structures are a complicated fabrication process and an expensive unit cost. In this paper, the boron emitter doping profile of a nanosized boron rich layer (BRL), for which the boron and oxygen concentrations are correlated, is optimized to fabricate high efficiency solar cells on an *n*-type substrate. Boron doping was carried out using a BBr_3 furnace with varying oxygen gas ratios and the surface was treated with acid etching. The effect of the oxygen on the nanosized BRL was analyzed using both FTIR spectroscopy and XPS, where by conductivity and the Si-B bond were observed for the three-fold and four-fold coordinated borons, respectively. The results showed that the oxygen quantities in the boron doped emitter and the nanosized BRL affected the characteristics of the solar cell. Regarding the solar cells that were fabricated using the boron emitter and shallow emitter (90 ohm/sq) processes, the open-circuit voltage increased by 54 mV and the short circuit current (J_{SC}) increased by 3.7 mA/cm^2. The J_{SC} increase was due to an increased quantum efficiency in the short wavelength range. The shallow emitter etch back process minimized the boron–oxygen defects in the doping profile.

Keywords: *N*-Type Solar Cell, Boron Emitter, B–O Complex, Boron Rich Layer.

1. INTRODUCTION

Currently, the maximal share occupied by *p*-type Si solar cell technology in the global photovoltaics (PV) market is ∼85% due to process simplicity and a guaranteed technological status.[1–3] The light induced degradation (LID) exerted by boron oxygen (B–O) complexes on *p*-type substrates, however, leads to a decrease in cell efficiency of between ∼0.2 and ∼0.5% after exposure to light, and even after storage in the dark,[4,5] eliminating bulk boron and/or oxygen from the silicon is an effective way to avoid the LID effect. *N*-type crystalline-silicone (c-Si) exhibits greater potential as a high-efficiency base material compared with *p*-type c-Si. The inherent advantages of *n*-type Si such as the absence of B–O-related degradation effects[6,7] and a higher tolerance to common impurities[8,9] result in a higher diffusion length at a corresponding impurity level. SunPower and Sanyo are companies that use the *n*-type substrate for mass production. The heterojunction-with-intrinsic-thin-layer (HIT) cell of Sanyo consists of a *p*+ emitter on an *n*-substrate that is textured by a deposited layer of *p*-doped amorphous silicon (a-Si); the rear surface is passivated by the c-Si to obtain the full potential of the mono-crystalline *n*-type cell. Sanyo achieved a conversion efficiency of 23.7%[10,11] with their HIT cell, but it is difficult to control the thickness, impurity density, interface condition, and uniformity when the deposition is made on a textured Si substrate. The interdigitated back-contact (IBC) solar cells of SunPower comprise metallic conductors on the rearside of the cell and the front side of the cell is thus fully exposed to the

---

[*] Author to whom correspondence should be addressed.

1533-4880/2016/16/4846/005 doi:10.1166/jnn.2016.12177

sunlight. The IBC design comprises a back p–n junction cell in which both the p and n contacts are in the form of interdigitated grids on the rear surface,[12] the IBC cell must therefore be fabricated on Si wafers with a long minority-carrier diffusion length. Also, the distance from any point in the cell to the junction must be far shorter than the diffusion length, while excellent front-surface passivation is a prerequisite. Although, to fabricate the SunPower IBC cell, a number of process steps are required as part of the fabrication process and such complexity is a market-entry barrier.

Numerous research studies have been undertaken to develop high-efficiency, n-type Si solar cells in a laboratory environment using cost-intensive processing steps, whereby most of the steps cannot be directly implemented in a mass-production context; therefore, industrially applicable, cost-effective processing steps that are compatible with the existing, affordable p-type Si solar-cell technology are required. A key task in this regard is the development of a boron emitter that adheres to an n-type substrate, while also being of an excellent standard and cost-effective. Lowering the surface concentration with in-situ oxygen flow (concentration/content) during boron doping is a simple way to achieve high efficiency. In this paper, the main idea is to reduce the B–O defects created during boron doping by removing the excess B–O complexes with an etch-back process.

2. EXPERIMENTAL DETAILS

Solar-grade, thin n-type Czochralski (Cz-Si) wafers of crystal orientation (100), a resistivity of 1.5 ohm-cm, and a thickness of 200 μm were used as the starting material for our cell fabrication. To reduce the reflectance of the silicon wafer, texturing was carried out with NaOH 2%, IPA 8.75%, a temperature from 84–86 °C and an etching time of 5 min. The resultant pyramid size was under 5 μm and the front-side emitter was formed by BBr_3 doping. The textured n-type c-Si wafers were doped with boron using a conventional thermal diffusion process in a furnace with BBr_3 as the dopant source, at 950 °C for 15 min; the doped wafers were then subject to a drive-in process for 30 min at 1,080 °C. The front-side-emitter-doped wafers were diffused using pentavalent impurity (phosphorus) to form an $n+$ back surface field, with a phosphoryl chloride ($POCl_3$) diffusion, at 830 °C for 7 min, serving as a pre-deposition; this was followed by a 25 min drive-in to improve the diffusion of the phosphorus. The removal of the borosilicate glass and phosphosilicate glass layers was carried out by a dipping in a diluted HF solution for 30 s, followed by a DI-water rinsing and drying. To optimize the boron-doped emitter, the emitter-sheet resistance was optimized using an etch-back method with two different solutions: a HF-HNO_3 mixture and a HF-HNO_3–CH_3COOH mixture. After emitter sheet resistance optimization, NaOH treatment to remove porous silicon layer. The PECVD process used SiH_4, NH_3, and Ar gases to deposit a front refractive index of 2.2 and a back refractive index of 2.7 onto the silicon nitride (SiNx) thin films. For metallization, front and rear electrodes were screen printed using Ag/Al and Ag pastes that were co-fired at varying temperatures inside a four-zone belt furnace.

The effective minority-carrier lifetimes (τ_{eff}) of the Si substrate were determined using a microwave photoconductance decay technique, whereby the WCT-120 lifetime measurement system was set to a quasi-steady-state photoconductance mode. The molecular vibration mode and functional groups for the boron-doped emitter and nanosized BRL were characterized by a FTIR spectroscopy (Prestige-21 spectrometer, Shimadzu). The XPS ESCA2000 (VG microtech) system, with a monochromatic Al K_α (1486.6 eV) source, was used to characterize the relative surface composition of the boron-doped emitter and nanosized BRL. The cells were then characterized after the fabrication of the solar cells was completed. The reflectance of the samples was analyzed in the wavelength region of 300–1100 nm using a QEX7-model IPCE (incident photon to current conversion efficiency) measurement system. The illuminated current–voltage (I–V) characteristics were measured under the global solar spectrum of 25 °C, air mass (AM) 1.5.

3. RESULTS AND DISCUSSION

To analyze the effect of the oxygen flow (concentration/content) during boron doping, a quantitative analysis of the boron and oxygen surface concentrations to the emitter junction depth was completed using SIMS;

Figure 1 shows the SIMS data for the boron and oxygen profiles. The boron surface concentration was 4×10^{19} cm^{-3} for the drive-in process in the oxygen environment; however, even though the sheet resistances were the same, the surface concentration was 1×10^{20} cm^{-3} for the process in the nitrogen environment. After processing in the nitrogen environment, the etch-back method was conducted to increase the sheet

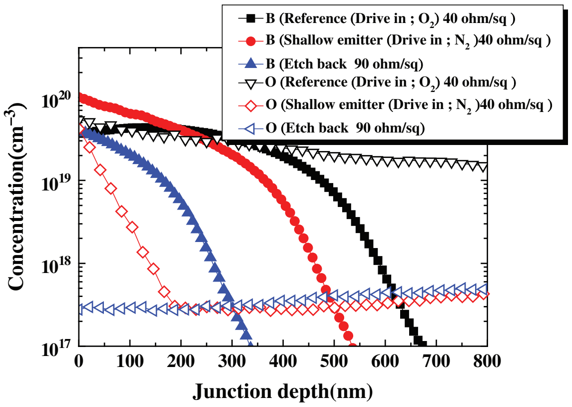

Figure 1. SIMS depth profile of boron and oxygen with varying oxygen quantities during the doping and etch-back processes.

resistance to 90 ohm/sq, decreasing the boron surface concentration to 4×10^{19} cm^{-3}. When the drive-in process was carried out in the oxygen environment, the oxygen surface concentration was 6×10^{19} cm^{-3} and gradually decreased to a bulk concentration of 1×10^{19} cm^{-3}. When processed in the nitrogen environment, the oxygen surface concentration was 5×10^{19} cm^{-3} before it dropped rapidly, and it then gradually increased to a bulk concentration of 1×10^{19} cm^{-3}. During the etch-back process, the highly concentrated oxygen was removed by etching, resulting in a low surface concentration of 3×10^{17} cm^{-3}.

Figure 2 shows the effect of oxygen flow (concentration/content) on B_4^- peak, oxygen content and conductivity. When the oxygen-gas ratio was decreased during the drive-in process, the peak of the B_4^- increased from 95 to 507, while the conductivity also increased, from 239 S/cm to 845 S/cm. The oxygen extracted from the FTIR analysis is depicted in Figure 3, and the transmittance from the FTIR data is converted to the absorption coefficient using the following equation. The oxygen can be extracted by integrating an absorption value of between 940 and 1090 nm and then multiplying it by a constant:[13, 14]

$$T = \frac{4T_0 2e^{-\alpha d}}{(1+T_0)^2 - (1-T_0)^2 e^{-2\alpha d}}$$

$$\rightarrow e^{-\alpha d} = \frac{-4T_0^2 \pm \sqrt{16T_0^4 - 4T^2(1-T_0^2)^2}}{2T(1-T_0)^2} \qquad (1)$$

$T_0 = 0.54(\alpha = 0)$

α = absorption coefficient

$\mathrm{C(O)} = \mathrm{A(O)I}(940 - 1080)$

C(O) = oxygen concentration (at.%)

d = film thickness

$\mathrm{A(O)} = 0.156\,\mathrm{at.\%/eVcm^{-1}}$

$I(940 - 1080)$ = integrated absorption

The drive-in process in the oxygen environment resulted in more than 30 (at.%) oxygen, which contributed to B–O bond formations and resulted in numerous defects.

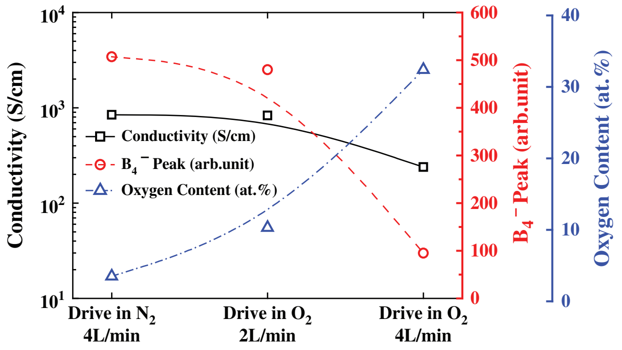

Figure 2. Conductivity, B_4^- peak, and oxygen quantities during the doping process.

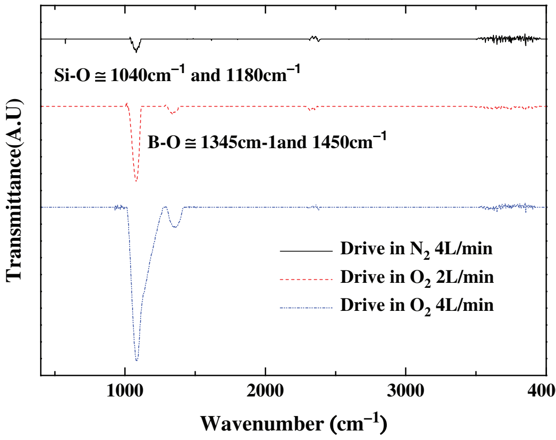

Figure 3. FTIR analysis of Si–O and B–O bonding with varying oxygen quantities during the doping process.

Figure 3 also shows the FTIR transmittance data of the samples processed under varying drive-in conditions; for silicon-monoxide (Si–O) bonds, symmetric stretching vibrations and asymmetric stretching vibrations are evident at 1040 and 1180 cm^{-1}, respectively, in this data. The B–O peaks appeared when asymmetric stretching vibrations occurred at 1345 and 1450 cm^{-1}. Only one Si–O peak appeared for the drive-in process in the nitrogen environment, while large Si–O and B–O peaks were seen for the drive-in process in the oxygen environment. As the oxygen-gas ratio increased, both the Si–O and B–O peaks increased; notably, the asymmetric stretching vibrations at 1180 cm^{-1} and the symmetric stretching vibrations at 1040 cm^{-1} overlapped. The existence and quantity of B–O bonds were affected by the condition of the drive-in process. The defects formed by the B–O bonds caused a degradation of the efficiency of the c-Si solar cells.[6, 15]

To investigate the effect of oxygen flow on Si-B bonds during boron doping, an XPS analysis was carried out and the results are shown in Figure 4. The B(1s) peak,

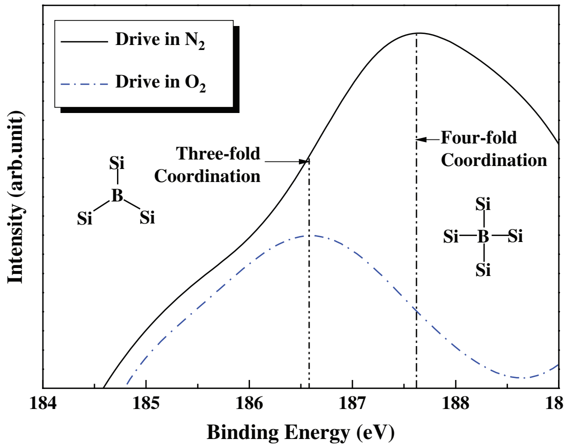

Figure 4. XPS analysis of four-fold-coordinated-boron (B_4^-) Si-B peak with nitrogen and oxygen quantities during the doping process.

obtained by fitting with Gaussian distribution, is the summation of the electronegativity near the silicon atoms, with the three-fold-coordinated boron and B_4^- appearing at 186.6 and 187.7 eV, respectively. The B(1s) peak shifted from the pure boron-binding energy value of 188 eV to a lower binding energy value due to the electronegativity. When the drive-in was performed in the nitrogen environment, the silicon boride (Si-B) bond of the B_4^- was dominant, as was confirmed at the peak of around 187.7 eV. The B_4^- remarkably decreased while the drive-in occurred in an oxygen environment, with a peak appearing at 188.6 eV, and, as the oxygen injection was decreased during the drive-in process, the B_4^- was increased; B_4^- is thus closely related to conductivity. The increase in B_4^- led to an increase of the positively-charged dangling bonds in accordance with the "8-N" doping rule; consequently, an increased B_4^- led to increased conductivity,[16, 17] as depicted in Figure 2.

To minimize the effect of the oxygen that produces B–O defects during boron doping, an etch-back process was conducted after doping; two different etching solutions (etchants) were used: $HF{:}HNO_3 = 1{:}100$ and $HF{:}HNO_3{:}CH_3COOH = 1{:}10{:}5$.

Figure 5 shows the minority-carrier lifetime and wet etching time as a function of the sheet resistance (R_s) variations with two different etchants. For the $HF{:}HNO_3 = 1{:}100$ etchant with an etching time of 20 s, a R_s of higher than 60 ohm/sq was attained; but, the lifetime started to deteriorate and this decrease can be attributed to the porous-like surface that was formed after the etching process. When the mirror polishing condition of $HF{:}HNO_3{:}CH_3COOH = 1{:}10{:}5$ was used, the R_s increased rapidly with a concurrent increase in lifetime; the initial lifetime increase was due to the BRL decrease. The $HF{:}HNO_3$ solution was not suitable for cell fabrication because the target R_s level could only be achieved after an overly long etching time; lifetime degradation increases as the etching time increases. The decrease of the recombination rate and defect density resulted in an increased current, as is shown in the following equations:

$$R_{\text{bulk}} = \frac{\Delta n}{\tau}, \quad R_{\text{surf}} = \frac{pn - n_i^2}{(n+n_1)/S_{P0} + (p+p_1)/S_{P0}} \tag{2}$$

$$\begin{aligned} n_1 &= n_i e^{(E_{\text{defect}} - E_i)/kT} \\ p_1 &= n_i e^{-(E_{\text{defect}} - E_i)/kT} \end{aligned} \tag{3}$$

where $\Delta n = n - n_0$; n is the electron-carrier concentration; n_0 is the electron concentration at thermal equilibrium; E_{defect} is the single defect level at energy; E_i is the intrinsic Fermi energy; and S_{n0} and S_{p0} are the electron and hole SRV parameters, respectively. In p–n junction solar cells, the surface recombination rate (R_{surf}) is an important factor for defining the recombination rate and current density relationship.[18] The resultant current density (J) is thus calculated as

$$\begin{aligned} |J| = q\left(\int_{\substack{\text{entire}\\ \text{cell}}} R_{\text{bulk}} \cdot d^3x + \int_{\substack{\text{cell}\\ \text{surface}}} R_{\text{surf}} \cdot d^2x\right) \\ - q\int_{\substack{\text{entire}\\ \text{cell}}} G(x) \cdot d^3x \end{aligned} \tag{4}$$

where $G(x)$ is the total generation rate in the cell. As shown in Eqs. (2)–(4), a close connection between carrier concentration, surface recombination, and total current density exists for p–n junction solar cells. The surface recombination rate and defect density were the dominant factors that determined the total current density in the etched-back solar cells.

Figure 6 shows the internal quantum efficiency (QE), while Table I shows the electrical parameters of the solar cells fabricated under different drive-in environment conditions, as well as with the etch-back process. The short wavelength range below 500 nm was largely affected by the surface recombination, while the drive-in process occurred in an oxygen environment, thereby resulting in a low QE.

As the junction depth deepened, the recombination rate of the dopant increased, reducing the QE in the short

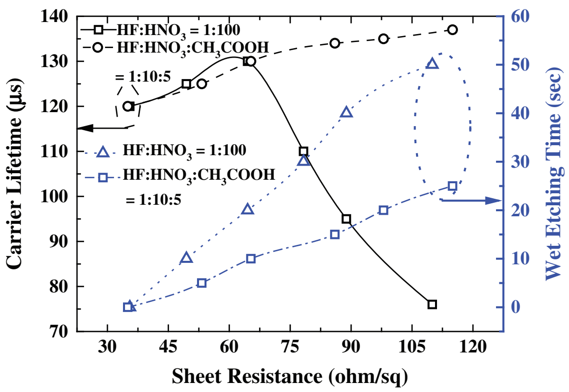

Figure 5. Variation in the carrier lifetime and wet etching time as a function of sheet resistance during etch-back process.

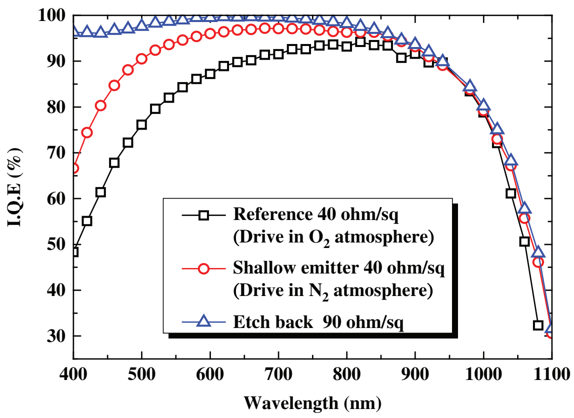

Figure 6. Internal Quantum Efficiency (IQE) of the solar cell fabricated with varying oxygen quantities during the doping and etch-back processes.

Table I. N-type c-Si solar cell parameters by varied condition of boron diffused layer.

Name	J_{SC} (mA/cm^2)	V_{OC} (mV)	FF (%)	Eff. (%)
Reference 40 ohm/sq	33.1	569	73.8	13.9
Shallow emitter 40 ohm/sq	35.4	613	71.2	15.5
Etched-back 90 ohm/sq	37.6	613	78.4	18.1

wavelength range. In the wavelength range of 500 nm $< \lambda <$ 900 nm, the internal QE became saturated near 100% for the drive-in process that occurred in a nitrogen environment and this can be attributed to the reduced recombination rate. The etch-back shallow-emitter profile that was formed by the nitrogen-environment drive-in process and subsequent etch-back process reduced the B–O defects, increased the B_4^- that increased conductivity, and decreased the recombination rate in the short wavelength range. From Table I, it is evident that the solar cells fabricated with the etch-back process increased the V_{OC} by 54 mV and the J_{SC} by 3.7 mA/cm^2, resulting in an improved efficiency.

4. CONCLUSION

The effect of oxidation on a boron-emitter doping profile was investigated for high-efficiency, n-type c-Si solar cells. The excess oxygen that was required to decompose the BBr_3 during the boron doping process resulted in B–O defects and decreased the $B4^-$ that contributed to conductivity, thereby resulting in a reduced efficiency. To overcome this problem, a nitrogen-environment drive-in process was applied to achieve a minimal bulk-oxygen concentration and a reduction of the boron–oxygen pair in the boron diffusion layer.

The remaining oxygen at the surface was removed with an etching process. As a result, the number of B–O defects was reduced, increasing the V_{OC}, while the shallow emitter reduced the recombination rate, increasing the J_{SC}; overall, a higher degree of efficiency was achieved. From this study, we can conclude that in-situ oxidation during the boron doping drive-in process formed an excessive bulk-oxygen concentration, resulting in a low efficiency. To optimize the doping profile, the use of a minimal-oxygen boron-doping process and an emitter etch-back process makes it possible to attain a high efficiency in a simple and effective manner.

Acknowledgment: This work was supported by the Human Resources Development program (No. 20144030200580) of the Korea Institute of Energy Technology Evaluation and Planning (KETEP) grant funded by the Korea government Ministry of Trade, Industry and Energy. This work was supported by the Global Excellent Technology Innovation of the Korea Institute of Energy Technology Evaluation and Planning (KETEP), granted financial resource from the Ministry of Trade, Industry and Energy, Republic of Korea (No. 20135020910050).

References and Notes

1. T. Saga, *NPG Asia Mater.* 2, 96 (**2010**).
2. D. Song, J. Xiong, Z. Hu, G. Li, H. Wang, H. An, B. Grenko, K. Borden, K. Sauer, T. Roessler, J. Cui, H. Wang, B. Yu, J. Bultman, A. H. Vlooswijk, and P. R. Venema, *Proceedings of the IEEE 38th Photovoltaic Specialists Conference*, Austin, Texas, USA (**2012**), pp. 3004–3008.
3. D. Neuhaus and A Munzer, *Advances in OptoElectronics* 2007, 1 (**2007**), Article ID 24521.
4. J. Knobloch, S. W. Glunz, D. Biro, W. Warta, E. Schaffer, and W. Wettling, *Proceedings of the 25th IEEE Photovoltaic Specialist Conference*, Washington, DC, USA (**1996**), pp. 405–408.
5. J. Zhao, A. Wang, and M. A. Green, *Prog. Photovolt: Res. Appl.* 8, 549 (**2000**).
6. K. Bothe, R. Sinton, and J. Schmidt, *Prog. Photovolt: Res. Appl.* 13, 287 (**2005**).
7. J. Schmid and K. Bothe, *Phys. Rev. B* 69, 024107 (**2004**).
8. J. Schmidt, A. G. Aberle, and R. Hezel, *Proceedings of the 26th IEEE Photovoltaic Specialists Conference*, Anaheim, CA (**1997**), pp. 13–18.
9. S. W. Glunz, S. Rein, J. Y. Lee, and W. Warta, *J. Appl. Phys.* 90, 2397 (**2001**).
10. T. Kinoshita, D. Fujishima, A. Yano, A. Ogane, S. Tohoda, K. Matsuyama, Y. Nakamura, N. Tokuoka, H. Kanno, H. Sakata, M. Taguchi, and E. Maruyama, *Proceedings of the 26th European Photovoltaic Solar Energy Conference*, Hamburg, Germany (**2011**), pp. 871–874.
11. M. Taguchi, Y. Tsunomura, H. Inoue, S. Taira, T. Nakashima, T. Baba, H. Sakata, and E. Maruyama, *Proceedings of the 24th EUPVSEC*, Hamburg, Germany (**2009**), pp. 1690–1693.
12. P. J. Cousins, D. D. Smith, H. C. Luan, J. Manning, T. D. Dennis, A. Waldhauer, K. E. Wilson, G. Harley, and G. P. Mulligan, *Proceedings of the 35th IEEE Photovoltaic Specialist Conference*, Hawaiian Convention Center, Honolulu, HI, USA (**2010**), pp. 823–826.
13. A. A. Langford, M. L. Fleet, B. P. Nelson, W. A. Lanford, and N. Maley, *Phys. Rev. B* 45, 13367 (**1992**).
14. K. Haga and H. Watanabe, *J. Non-Crystalline Solids* 195, 72 (**1966**).
15. S. W. Glunz, J. Benick, D. Biro, M. Bivour, M. Hermle, D. Pysch, M. Rauer, C. Reichel, A. Richter, M. Rudiger, C. Schmiga, D. Suwito, A. Wolf, and R. Preu, *Proceedings of the 35th PVSC* (**2010**), pp. 50–56.
16. R. A. Street, *Phys. Rev. Lett.* 49, 1187 (**1982**).
17. T. Kazahaya and M. Hirose, *Jpn. J. Appl. Phys.* 25, L75 (**1986**).
18. S. J. Robinson, A. G. Aberle, and M. A. Green, *IEEE Trans. Electron Devices* 41, 1556 (**1994**).

Received: 17 February 2015. Accepted: 1 June 2015.